Recurrent Cometary Activity in Near-Earth Object (3552) Don Quixote

Michael Mommert[1] , Joseph L. Hora[2] , David E. Trilling[3] , Nicolas Biver[4], Kacper Wierzchos[5] , Olga Harrington Pinto[6],
Jessica Agarwal[7] , Yoonyoung Kim[7] , Andrew McNeill[3], Maria Womack[8] , Matthew M. Knight[9,10] , David Polishook[11],
Nick Moskovitz[1] , Michael S. P. Kelley[9] , and Howard A. Smith[2]

[1] Lowell Observatory, 1400 W Mars Hill Rd, Flagstaff, AZ 86001, USA; michael.mommert@lowell.edu
[2] Harvard-Smithsonian Center for Astrophysics, 60 Garden St, Cambridge, MA 02138-1516, USA
[3] Department of Astronomy and Planetary Science, Northern Arizona University, P.O. Box 6010, Flagstaff, AZ 86011, USA
[4] LESIA Observatoire de Paris, 5 pl. J. Janssen, F-92190 Meudon, France
[5] Catalina Sky Survey, Lunar and Planetary Laboratory, University of Arizona, Tucson, AZ 85721, USA
[6] Department of Physics, University of Central Florida, Orlando, FL 32816, USA
[7] Max Planck Institute for Solar System Research, Justus-von-Liebig-Weg 3, D-37077 Göttingen, Germany
[8] Florida Space Institute and Department of Physics, University of Central Florida, Orlando, FL 32816-2385, USA
[9] University of Maryland, 1113 Physical Sciences Complex, Building 415, College Park, MD 20742-2421, USA
[10] Department of Physics, United States Naval Academy, 572C Holloway Rd, Annapolis, MD 21402, USA
[11] Faculty of Physics, Weizmann Institute of Science, Rehovot 0076100, Israel

Abstract

We report on observations of activity in near-Earth object (3552) Don Quixote using the Spitzer Space Telescope and ground-based telescopes around its 2018 perihelion passage. Spitzer observations obtained six months before perihelion show extended emission around the target's nucleus that is most likely caused by molecular band emission from either CO_2 or CO, but we find no significant emission from dust. Ground-based optical observations taken close to perihelion reveal for the first time activity in the optical wavelengths, which we attribute to solar light reflected from dust particles. IRAM millimeter radio observations taken around the same time are unable to rule out CO as the driver of the molecular band emission observed with Spitzer. The comparison of the gas activity presented here with observations performed during Don Quixote's previous apparition suggests that activity in Don Quixote is recurrent. We conclude that (3552) Don Quixote is most likely a weakly active comet.

Unified Astronomy Thesaurus concepts: Small solar system bodies (1469); Near-Earth objects (1092); Comet nuclei (2160); Infrared astronomy (786); Millimeter astronomy (1061); Optical observatories (1170)

1. Introduction

Near-Earth object 3552 Don Quixote (1983 SA) was discovered on 1983 September 26 by P. Wild. Despite its apparently comet-like orbit (Hahn & Rickman 1985; Bottke et al. 2002), the lack of a tail led to its classification as an asteroid. Physical characterization over the following years revealed further hints at a potentially cometary origin of this body: using thermal-infrared observations, Veeder et al. (1989) found a low, comet-like, surface albedo, which was later confirmed with Spitzer Space Telescope observations (Mommert et al. 2014), and spectroscopic observations found a reflective behavior most similar to D-type asteroids (Hartmann et al. 1987; Binzel et al. 2004; Mommert et al. 2014), which in turn resembles the spectra of comets (DeMeo & Binzel 2008). Recent observations of Don Quixote characterize this object as having an effective diameter of $18.4^{+0.3}_{-0.4}$ km and a geometric albedo $p_V = 0.03^{+0.02}_{-0.01}$ (Mommert et al. 2014), as well as a rotational period of 6.665 hr (Skiff et al. 2019). Furthermore, simulations by Rudawska & Vaubaillon (2015) find correlations between the orbit of Don Quixote and observed meteor streams. All of these observations hint toward a cometary nature of this body.

Mommert et al. (2014) were the first to report cometary activity in this object based on Spitzer Space Telescope observations taken in 2009. They observed extended emission in Spitzer IRAC Channel 2 (4.5 μm) but a lack of activity in Channel 1 (3.6 μm), which they attribute to the outgassing of CO_2 or CO from the surface of Don Quixote. Due to the singular nature of this observation and the fact that at that time activity had never been observed in the optical, they attributed the observed activity to a short outburst, potentially caused by a recent impact exposing subsurface volatiles.

In order to test hypotheses for the nature of activity observed in Don Quixote, we obtained additional observations around its perihelion passage on 2018 May 8 in the framework of the program "Systematic Characterization of and Search for Activity in Potentially Active Asteroids" (see Mommert et al. 2020 for details and results). We present here observations of Don Quixote taken with the Spitzer Space Telescope and using ground-based optical and millimeter telescopes.

2. Observations and Image Analysis

We obtained observations of Don Quixote with the Spitzer Space Telescope, a range of ground-based optical telescopes, and the IRAM 30 m millimeter radio telescope. Ground-based observations were triggered by the results of the Spitzer observations presented here. Relevant observation details are listed in Table 1.

2.1. Spitzer Space Telescope

We observed Don Quixote with the IRAC instrument (Fazio et al. 2004) on board the Spitzer Space Telescope (Werner et al. 2004) during its warm mission phase as part of the Cycle 13 DDT

Table 1
Table of Observations

Observatory	Midtime	r (au)	Δ (au)	ν (deg)	α (deg)
Spitzer	2017 Oct 1 22:07	2.72	2.60	251.8	21.9
SOAR	2018 Mar 26 09:37	1.35	1.63	322.9	37.7
SOAR	2018 Apr 25 09:26	1.25	1.53	348.7	40.8
IRAM 30 m	2018 Jun 10 07:12	1.31	1.51	30.2	41.5
Magellan Baade	2018 Jun 22 09:38	1.37	1.50	39.9	41.1

Note. For each observation we list the observatory name, the observation midtime in UT, the target's heliocentric distance, the distance from the observer, the true anomaly, and the solar phase angle.

program "Spitzer identification of potentially active Near-Earth Asteroids" (PID 13164). The observations (Astronomical Observation Request, AOR 63156224) took place between 2017 October 1 18:04:51 UT and 2017 October 2 02:10:31 UT for a total of 8.08 hr clock time and a total integration time of 6.1 hr (220 individual frames with 100 s frames in High Dynamic Range mode) for both bands. At the time of the observations, Don Quixote was inbound in its orbit with a heliocentric distance of 2.72 au and 2.60 au from Spitzer. Don Quixote was observed at a solar phase angle of 21°.9 and true anomaly of 251°.9. Don Quixote moved a total of 2′.4 during our observations.

The AOR used the "Moving Cluster" mode and alternately placed the target on the 3.6 μm (IRAC CH1) and 4.5 μm (IRAC CH2) array. A medium dither pattern was used to enable background subtraction. Mosaics in both bands were constructed using the IRACproc software (Schuster et al. 2006) in the moving frame of the target. The final mosaics are presented in the left column of Figure 1.

To search for extended emission around the target, we perform a Point-Response-Function (PRF) subtraction in both IRAC channels. In this subtraction, we use the warm mission PRFs (Hora et al. 2012) as a model, scale it to the target's PRF, and subsequently subtract the fitted models (see Mommert et al. 2014, for details). The PRF-subtracted mosaics shown in the center column of Figure 1 clearly show extended emission at 4.5 μm but not so at 3.6 μm; irregularities near the nucleus are the result of over-subtractions caused by imperfect placement and intensity scaling of the PRF. The results of this work are not affected by these imperfections, as they are based on radial brightness profile measurements that explicitly ignore these areas.

2.2. Ground-based Optical Observations

We obtained repeated observations of Don Quixote during semesters 2015A through 2019B with a range of observatories, none of which show definitive signs of activity in the form of extended emission around the target. However, observations taken at heliocentric distances less than 3 au show signs of brightening (see Mommert et al. 2020 for details).

In this work, we present additional observations that, for the first time, show comet-like activity around Don Quixote at optical wavelengths. The first such observation was obtained with the Southern Astrophysical Research Telescope (SOAR) and its Goodman High Throughput Spectrograph (Clemens et al. 2004) in imaging mode in the framework of the "Mission Accessible Near-Earth Objects Survey"[12] (MANOS). Don Quixote was observed on 2018 March 26 in the astronomical

twilight hours from 09:37 to 09:44 UT using a VR broadband filter, resulting in 22 frames each with an exposure time of 10 s. Despite increasing background brightness levels, passing clouds, and seeing around 3″ FWHM, extended emission around the target is apparent and has been reported by Mommert et al. (2018).

Follow-up observations were taken with the same instrument on 2018 April 25, between 09:14 and 10:04 UT, ending during astronomical twilight and with better seeing of around 2″ FWHM. We obtained 33 frames with 30 s integration time each and using the VR broadband filter. The data show a distinct coma and a faint tail emerging from the nucleus.

We obtained additional observations with the Magellan Baade Telescope using the Inamori-Magellan Areal Camera and Spectrograph (IMACS) in imaging mode. On 2018 June 22, 48 V-band frames with exposure times of 40 s were taken between 09:38 and 10:40 UT. These observations suffer from extremely high background levels due to cirrus and a bright Moon at 70% illumination. The seeing at the time of observations was around 1″.5 FWHM.

We stack each set of observations in the moving frame of the target to remove background sources and improve the signal-to-noise ratio of cometary features. To prepare the data, we manually improve the World Coordinate System information in each frame based on the Gaia DR2 catalog (Brown et al. 2018). Image stacking is performed using `photometrypipeline` (Mommert 2017), which in turn relies on SWARP (Bertin et al. 2002) using a clipped average combination; background levels were subtracted from each frame before combination. We produce a "comove" image that is stacked in the moving frame of the target and a "skycoadd" image in the rest frame of the background. In the case of the comove image, bright sources other than Don Quixote are masked by replacing pixels brighter than a threshold with the median pixel value across the image. Comove images are shown in the left column of Figure 2.

We measure the azimuthally averaged radial brightness distribution around Don Quixote from the comove image and do the same for a similarly bright star from the skycoadd image. We scale the latter distribution to the former by multiplying it with a scalar factor and subtract it from the comove image to improve the visibility of morphological structure in the coma. We show the subtracted comove in the center column of Figure 2 and the radial brightness profiles in the right column.

We also use the skycoadd images to obtain a photometric calibration of our comove images using `photometrypipeline`. Photometric calibration is based on the magnitudes of field stars with solar-like colors extracted from the Gaia DR2 catalog (Brown et al. 2018) and transformed to V magnitudes using the transformations provided by the Gaia DR2
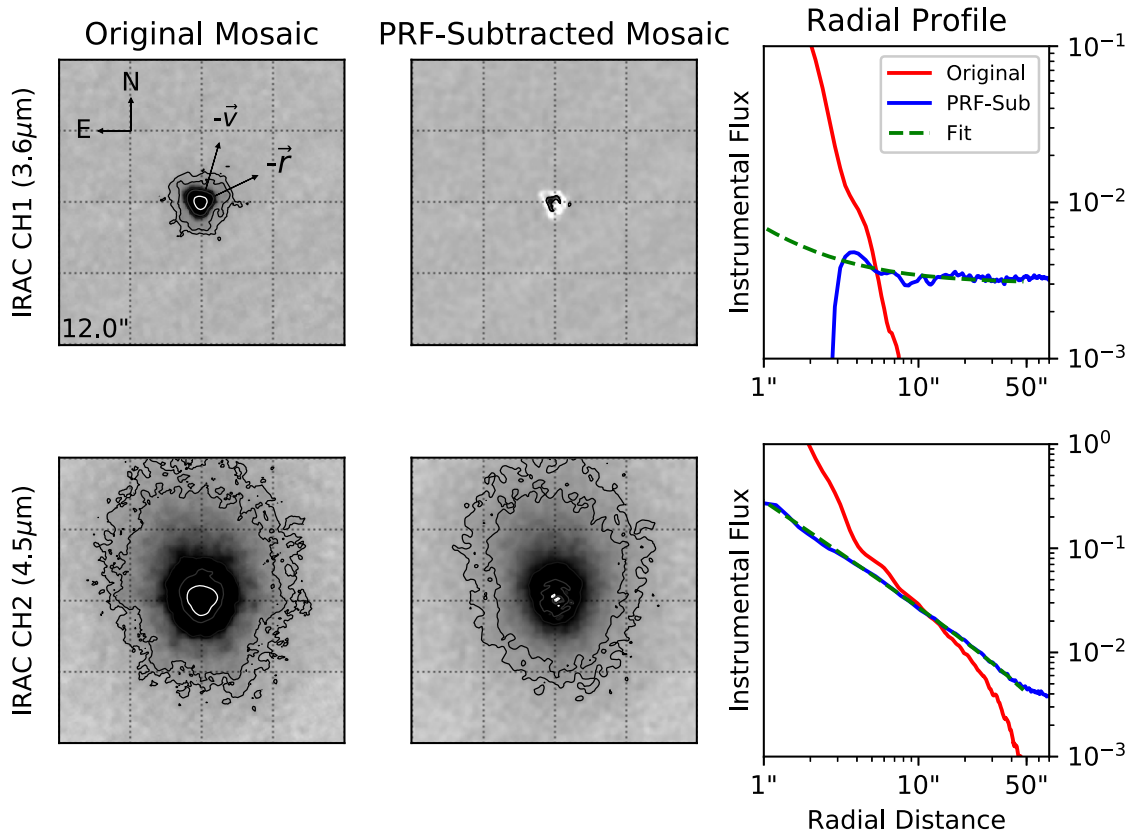
---

[12] https://manos.lowell.edu

Figure 1. Spitzer IRAC mosaics (inverted grayscale): the left column shows original mosaics, PRF-subtracted mosaics are shown in the center column, and the right column presents radial profiles derived from the different mosaics in instrumental flux density units. All mosaics share the same linear scaling; contour lines are plotted to distinguish discrete flux levels at [0.005, 0.01, 0.05, 0.1, 0.5] MJy Sr^{-1} and are shown in shades of gray ranging from black to white. Each mosaic covers $48'' \times 48''$ on the sky (91×10^3 km at the target distance), and the orientation in the plane of the sky, the direction to the Sun ($-\boldsymbol{r}$), and the inverse of the target's velocity vector ($-\boldsymbol{v}$) are indicated. The 4.5 μm mosaics clearly show extended emission, whereas the target appears as a point source at 3.6 μm (see Section 3.2.1). This is reflected by the radial profile plots that show extended emission in the PRF-subtracted brightness profile (blue line) at 4.5 μm, but not at 3.6 μm. The red lines represent the radial brightness profile from the original mosaics and the dashed lines represent a fit to the PRF-subtracted profile. The dashed green line represents a fit to the outer parts of the PRF-subtracted brightness profile that is extrapolated to the inner parts of the coma.

documentation. In the case of our Magellan observations, only a few field stars were available for calibration, none of which had solar-like colors; in this case we reverted to adopting the magnitude zero-point based on all available stars and adopted a total uncertainty on the zero-point of 0.3 mag to account for this fact.

2.3. Ground-based Millimeter Radio Observations

We obtained observations using the IRAM 30 m antenna in search for emission from the CO (2–1) transition at 230.538 GHz between 2018 June 8 04:50 UT and 2018 June 12 09:40 UT, amounting to a total of 21 hr on target. The observations were conducted with the EMIR receiver and the VESPA autocorrelator and the fast Fourier transform spectrometer (FTS) backends, which provided spectral sampling of 20 and 200 KHz per channel, respectively. When converted to Doppler velocity, the spectral resolutions are 0.026 km s^{-1} for VESPA and 0.254 km s^{-1} for FTS. At 230 GHz, the half-power beamwidth diameter of the IRAM 30 m antenna is $\theta = 10\rlap{.}''5$, which corresponds to 11,500 km at the object's distance during the observations. We used the JPL Horizons ephemeris (Giorgini et al. 1996) to track Don Quixote and the pointing of the telescope was checked against bright sources like Uranus. We estimated the rms pointing error to be $1\rlap{.}''4$. The data were reduced and analyzed using the GILDAS

software. Due to transparency issues during our observations as well as time lost to weather our observations are limited in sensitivity.

3. Results

3.1. Qualitative Analysis of the Observed Activity

Figure 3 shows Don Quixote's orbit and observations considered in this work. We supplement our data with data from Mommert et al. (2014, 2020) and find that all observations that clearly show comet-like activity in the form of extended emission (this work and Mommert et al. 2014) or unusual photometric brightening (labeled as "likely active," data from Mommert et al. 2020) occur at heliocentric distances less than 3 au, which corresponds to true anomalies of $\pm115°$.

In agreement with previous Spitzer Space Telescope observations of Don Quixote (Mommert et al. 2014), we find extended emission around the nucleus in CH2 at 4.5 μm, but not so in CH1 at 3.6 μm (see Section 2.1.) If dust were present in these observations, any emission in CH1 could be attributed to sunlight reflected off dust particles, while emission in CH2 consists of a mixture of thermal emission from dust and reflected sunlight (Reach et al. 2013). Given the lack of emission in CH1, the extended emission in CH2 can instead be attributed to molecular band emission in the CH2 bandpass from vibrational molecular transitions of either CO_2 or CO
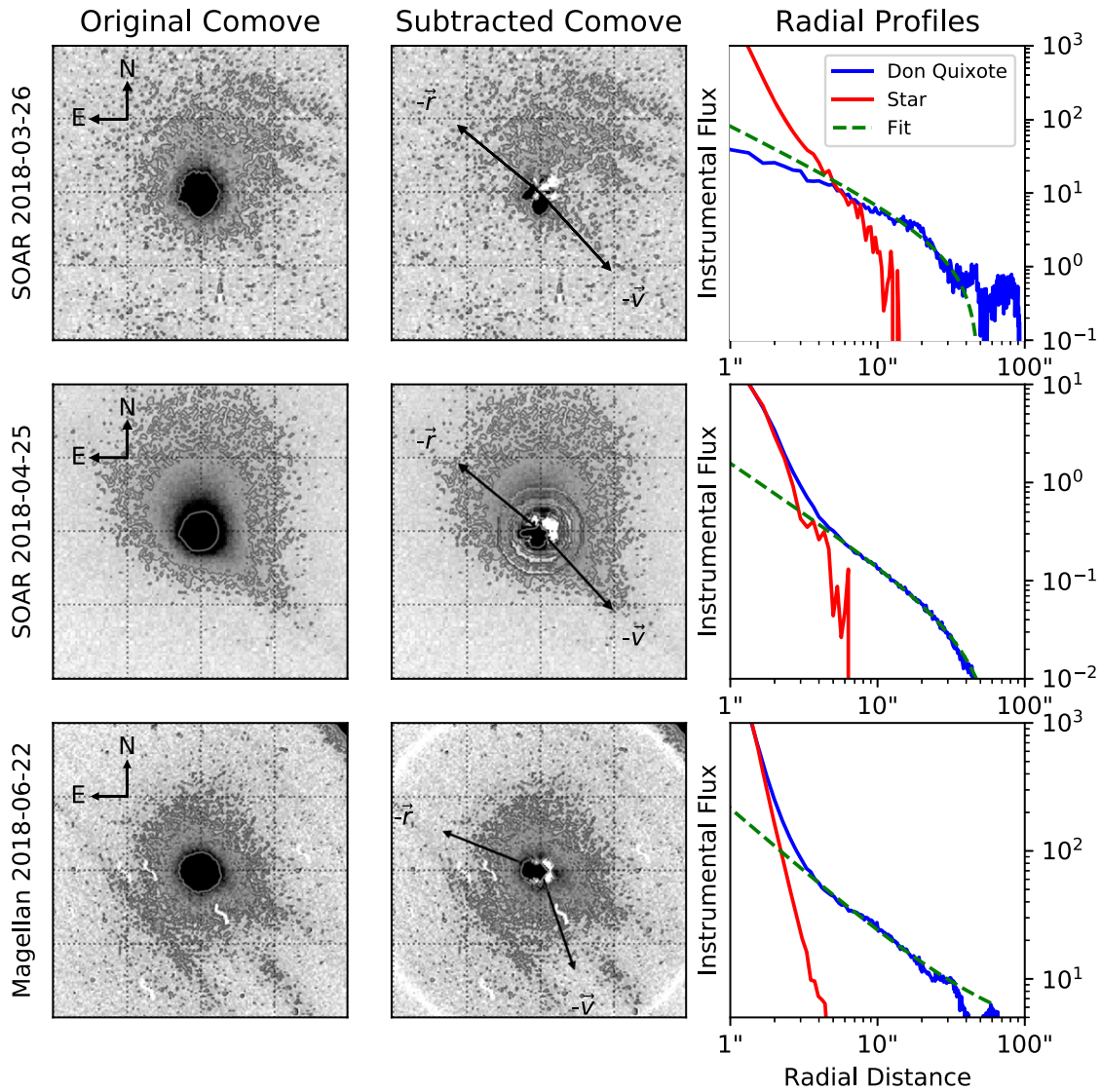
Figure 2. Optical detections of activity in Don Quixote. The left column shows stacked images in the comoving frame of the target ("Original Comove"), the center column shows the same images from which the radial brightness profile of a star has been subtracted ("Subtracted Comove"), and the right column plots radial brightness profiles for Don Quixote (blue) and a star (red) using a log-log scale (with instrumental flux density units on the y-axis). Field orientation, as well as the direction to the Sun ($-r$), and the projection of the negative velocity vector ($-v$) are indicated in the original comove plots. Each mosaic spans $40''$ on one side (47×10^3 km for the SOAR 2018 March 26 observations, 44×10^3 km for the SOAR 2018 April 25 observations, and 44×10^3 km for the Magellan 2018 June 22 observations at the target distance), and the image scale is inverted and linear; contour lines in the original and subtracted comoves are the same on each line. The green dashed line in the right column represents a fit to the outer parts of the radial brightness distribution of Don Quixote that is not affected by the star-like nucleus.

(A'Hearn et al. 2012; Ootsubo et al. 2012; Reach et al. 2013; Mommert et al. 2014). The lack of emission in CH1 thus points to a lack of significant amounts of dust in these observations, which would be about equally detectable in both channels since scattered sunlight dominates over thermal emission at 2.7 au. We apply a number of comet coma enhancement techniques (division by azimuthal average, azimuthal renormalization, and division by $1/\rho$ profile as implemented by Samarasinha et al. 2013) to the PRF-subtracted CH2 data and find the observed emission to be stronger in the parts north of the nucleus, as already suggested by the contour lines in Figure 1. We do not find clear fans, focused jets, or other morphological features in the coma.

Deep optical observations using SOAR and Magellan at the time of the 2018 perihelion passage show for the first time extended emission in the optical wavelengths. These observations took place within $\sim$0.1 au of the target's minimum distance to the Sun, while observations at larger distances show no extended emission but excess brightness that might hint to ongoing activity (Mommert et al. 2020). Similar to our Spitzer observations, the application of comet coma enhancement techniques reveals that the observed emission is slightly stronger north of the nucleus of Don Quixote in each of our ground-based observations (see Figure 2). Only our SOAR observations obtained on 2018 April 25, when the target was closest to the Sun, show a faint tail pointing to $\sim$220° east of north (see Figure 2, center row).

3.2. Quantitative Analysis and Production Rates

3.2.1. Dust and Gas Production Rates from Spitzer

In order to quantify the dust and gas production during our Spitzer Space Telescope observations, we measure the flux
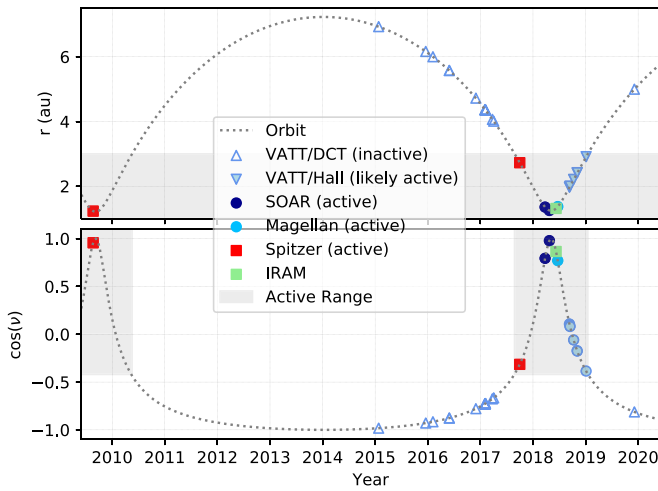
Figure 3. Observations of Don Quixote considered in this work. We plot heliocentric distance as a function of time (top plot) and the cosine of the target's true anomaly as a function of time (bottom plot). We find that all observations during periods in which Don Quixote showed signs of activity happen at heliocentric distances within 3 au of the Sun, which corresponds to true anomalies $\pm 115°$ ($\cos(\pm 115) = -0.42$). This figure includes data from Mommert et al. (2014) and Mommert et al. (2020).

densities emitted by the coma in CH2 and establish an upper limit for potential emission in CH1. For that purpose, we fit a function of the form $F(\rho) = a/\rho + b$ to the PRF-subtracted radial brightness profiles in Channel 1 and Channel 2 (see Figure 1), where ρ is the distance to the nucleus of Don Quixote in arcseconds and a and b are fit parameters, as expected for an optically thin cometary coma produced from constant outgassing. We find a best-fit slope parameter $a \sim 1.2$. Flux densities in CH1 and CH2 follow from integration over these profiles in a circular aperture with radius $7{''}5$ after subtraction of the background signal, which we derive as the average signal from parts of the mosaics that are close to the target but not affected by extended emission. We account for the extended nature of the emission by applying the IRAC extended source photometrical correction coefficients (Spitzer Science Center 2012) and find a flux density of 264 ± 11 μJy in CH2, but only an upper-limit estimate (1σ) of 13 μJy for the flux density in CH1.

Using the same methodology as used by Mommert et al. (2014; see Equations (1)–(5) and references therein), we derive upper limits on the dust production rate from the upper-limit flux density measured in CH1 and an estimate of the CO and CO_2 gas production rates from the CH2 flux density. Using the formalism introduced by A'Hearn et al. (1984), we estimate a 3σ upper limit $Af\rho_{CH1,3\sigma} = 22$ cm in CH1 and derive $Af\rho_{CH2} = 133 \pm 6$ cm in CH2 (see Mommert et al. 2014 for details). $Af\rho_{CH1,3\sigma}$ corresponds to an average surface brightness of 24.4 mag arcsec^2 in the V band as measured in a circular aperture with radius $7{''}5$.

We explore the upper limit on the dust production rate using the following assumptions: a dust particle bulk density of 500 kg m^{-3}, which is an average over constraints from different Rosetta instruments (Fulle et al. 2016; Hornung et al. 2016); a fixed particle size of 100 μm, which is compatible with observations of comet 67P/Churyumov–Gerasimenko at 3.4–3.7 au pre-perihelion (Rotundi et al. 2015); a geometric albedo of 0.03 (Mommert et al. 2014);

and a dust velocity of 10 m s^{-1} (see Section 3.3). From our upper limit on $Af\rho_{CH1,3\sigma}$ we thus derive a 3σ upper limit on the dust production rate of 2 kg s^{-1}. This level of dust activity, if real, would correspond to $\sim 1/6$ of the flux density measured in CH2. For comparison, a particle size of 10 μm results in a dust production rate upper limit (3σ) of 0.2 kg s^{-1}.

We finally estimate the production rate for CO_2. To correct for potential flux density contaminations from solar light reflected off dust in CH2, we subtract the estimated contribution from the measured CH2 flux density of the coma. Assuming a gas velocity of 0.49 km s^{-1} (Ootsubo et al. 2012) we estimate the CO_2 production rate using a single-species Haser model (Haser 1957; Mommert et al. 2014) and find a production rate of $(2.6 \pm 0.4) \times 10^{25}$ molecules s^{-1}.

In case the observed activity stems from the sublimation of CO instead of CO_2, we expect a CO production rate of $(2.6 \pm 0.4) \times 10^{26}$ molecules s^{-1} based on the ratio of the CO_2 and CO fluorescence efficiencies (Crovisier & Encrenaz 1983).

3.2.2. CO Production Rates from IRAM

In our IRAM observations, no CO (2–1) line was detected, but a 3σ upper limit of $Q(CO) < 10^{27}$ molecules s^{-1} was calculated. The limit was derived following the method described by Crovisier (1987), using the observed rms of 12.5 mK km s^{-1} in a spectral window of 1.7 km s^{-1}, a gas expansion velocity of 0.7 km s^{-1} (Ootsubo et al. 2012), and a kinetic temperature of $T = 30–40$ K.

3.2.3. Dust Production Rates from Optical Observations

We estimate dust production rates from our SOAR and Magellan observations using the same method used in Section 3.2.1. Coma flux densities are derived by integrating fits of the form $F(\rho) = a/\rho + b$ to the radial brightness distributions of Don Quixote at distances greater than $5{''}$ at which the radial brightness distribution is not affected by the star-like nucleus of the target (see Figure 2). We subtract the integrated average background from these flux densities. Accounting for observation circumstances, we find values for $Af\rho$ (V band) of (5.4 ± 0.5) cm, (7.3 ± 0.4) cm, and (3 ± 1) cm, for our SOAR 2018 March 26, SOAR 2018 April 25, and Magellan 2018 June 22 observations, respectively.

Using the same formalism and assumptions as in Section 3.2.1 (dust particle bulk density of 500 kg m^{-3}, a fixed dust particle size of 100 μm, a geometric albedo of 0.03 (Mommert et al. 2014), and a dust velocity of 10 m s^{-1}), we find dust production rates of (0.6 ± 0.1) kg s^{-1}, (0.8 ± 0.1) kg s^{-1}, and (0.4 ± 0.1) kg s^{-1} for our SOAR 2018 March 26, SOAR 2018 April 25, and Magellan 2018 June 22 observations, respectively.

3.3. Coma Dust Velocity and Particle Sizes

3.3.1. Velocity from Radial Brightness Profiles

The three optical observations obtained between 2018 March and June (Figure 2) show Don Quixote surrounded by an extended coma. In March and April, this coma is somewhat brighter or more extended in the Sun-facing hemisphere than on the nightside. Its shape is similar to the coma observed with Spitzer that likely contains CO or CO_2 (Section 3.2.1). The visible light is unlikely to stem from CO or CO_2, because these

molecules do not have significant emission lines in the observed wavelength range (VR and V, respectively). It cannot be excluded that the extended coma is (in part or fully) due to the presence of molecules like C_2 and NH_2, which have emission lines located in V band (Meech & Svoreň 2004). However, the more standard interpretation is that the light observed in the broad optical bandpasses is sunlight scattered by dust.

The radial profiles shown in the right column of Figure 2 have a slope parameter $a \sim 1$ in the aperture range that is not affected by light from the central point source but still inside the steep brightness drop at large apertures. Hence the coma surface brightness is inversely proportional to the radial distance (ρ) from the nucleus, as would be expected for a coma in steady state. However, the radial profiles drop much more steeply than $1/\rho$ for distances $\rho > \rho_0$. The deviation from a steady-state coma begins at around $20''$ in our two SOAR observations ($\rho_0 \sim 23,000$ km) and further out ($\sim 30''$, $\rho_0 \sim 33,000$ km) in our Magellan observations. The distance ρ_0 may be interpreted as the position at the time of observation of the slowest particles with a significant scattering cross section emitted (at speed v_{min}) at the point in time when the activity reached a steady state.

The difference in coma size, $\Delta\rho_0 = 10,000$ km, between our Magellan and SOAR observations can be used to estimate v_{min}. The times between observations is $\Delta T_{JM} = 76$ days between March and June, and $\Delta T_{JA} = 46$ days between April and June. This gives minimum velocities in the range $v_{min} = (1.5–2.5)$ m s^{-1}, well below the 5 m s^{-1} surface escape speed from a 9.2 km radius body having a typical cometary density of 500 kg m^{-3} (Pätzold et al. 2016). These particles may have left the surface at barely more than escape speed and lost a significant fraction of their kinetic energy when overcoming the nucleus gravity. The Hill radius of such a body at a heliocentric distance of 1.3 au is about 1300 km, hence $\sim 1''$ and not resolved.

The results of this analysis strongly depend on the measurement of ρ_0, which in turn depends on the proper subtraction of the PRF from each observation (Figure 2, center column). We test the robustness of v_{min} and the measurement of ρ_0 by shifting the PRF relative to the comove image on the order of 10 pixels, introducing a clearly bipolar pattern in the resulting surface brightness of the coma. Even in such extreme cases of flawed PRF subtraction, which would be easy to identify and dismiss, measurements of ρ_0 are within $\sim 20\%$ of the values derived above. Propagating these uncertainties leads to a $\sim 30\%$ uncertainty in v_{min}.

Based on this estimate of v_{min}, we adopt a dust velocity estimate in our dust production rate calculations (Sections 3.2.1 and 3.2.3) of 10 m s^{-1}, which agrees with our lower limit and its uncertainty, but is somewhat more conservative than the lowest velocity case.

Assuming that these particles have been traveling at constant speed after leaving the Hill sphere, they would have been emitted between late 2017 September ($r = 2.7$ au) and 2018 mid-January ($r = 1.9$ au). In this interpretation, these dates constrain the onset of dust activity in Don Quixote.

3.3.2. Dust Velocity and Particle Sizes from Coma Morphology

The coma extends to all directions from the nucleus and is more pronounced on the Sun-facing side. It does not smoothly
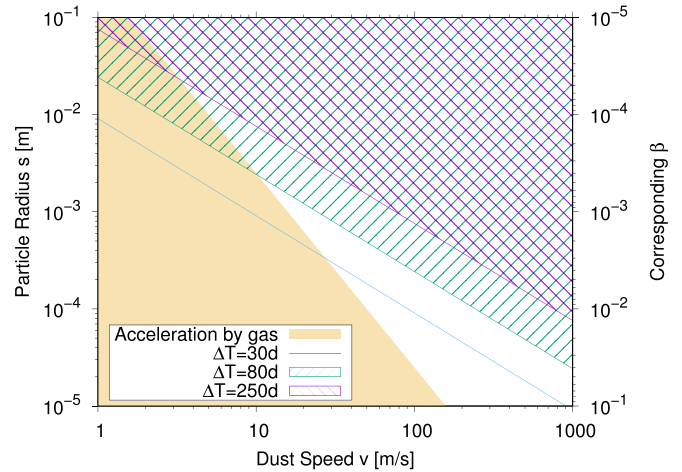

Figure 4. Illustration of two separate constraints on the dust size–velocity relation in Don Quixote. The yellow area shows which particle sizes can be accelerated to a given speed by gas drag, assuming that $v(s) = v_0 \times 10^{-3} s^{-0.5}$. We assume that the speed of $s = 1$ μm particles is $v_0 < 500$ m s^{-1}. The areas above the blue (not hatched for clarity), green and violet lines represent Equation (1) for $\Delta T = 30$, 80, and 250 days, respectively. The intersection between the yellow and one of the hatched areas gives the range of possible sizes and speeds for the given value of ΔT.

transit into an equally broad tail; instead, we find a faint, narrow tail in our 2018 April 25 SOAR observations that is discussed below. This lack of a broad tail indicates that the material is not strongly affected by solar radiation pressure that would push the dust in the direction opposite to the Sun. The strength of radiation pressure is usually characterized by the dimensionless parameter β that describes the ratio between solar radiation pressure and solar gravity acting on a particle (Burns et al. 1979). The parameter β is independent of the heliocentric distance but related to particle properties as $\beta = 5.7 \times 10^{-4} Q_{pr}/(\rho_d s)$, where Q_{pr} is the radiation pressure efficiency factor, ρ_d is the dust bulk density, and s is the radius of a spherical particle. In the following, we assume $Q_{pr} \sim 1$ and $\rho_d = 500$ kg m^{-3}.

The radiation pressure acceleration on a particle with given β at heliocentric distance r is therefore $a_{rp} = \beta GM_\odot / r^2$, where G is the gravitational constant and $M_\odot$ the mass of the Sun. For the trajectory of a particle traveling at a speed v to not be significantly affected by solar radiation pressure on the timescale ΔT, the condition $\Delta T a_{rp} \ll v$ must be fulfilled, or

$$s \gg 5.7 \times 10^{-4} \frac{Q_{pr}}{\rho_d} \frac{GM_{sun}}{r^2} \frac{\Delta T}{v}. \qquad (1)$$

This relation is illustrated in Figure 4 for $\Delta T = 30$, 80, and 250 days and velocities between 1 and 1000 m s^{-1}. Also shown is the area in size–velocity space that can be filled with standard assumptions about dust acceleration by gas drag in comets, which is essentially limited by the speed of the gas (~ 500 m s^{-1}) and follows an inverse square-root relation. Both conditions can be fulfilled simultaneously only for a combination of comparatively large sizes and small speeds. Given that radiation pressure does not seem to affect the coma shape on the 80 day timescale of our optical observations, we conclude that the particles containing most of the scattering cross section in the coma should be larger than a millimeter and have speeds <10 m s^{-1}, which is consistent with the result of Section 3.3.1.
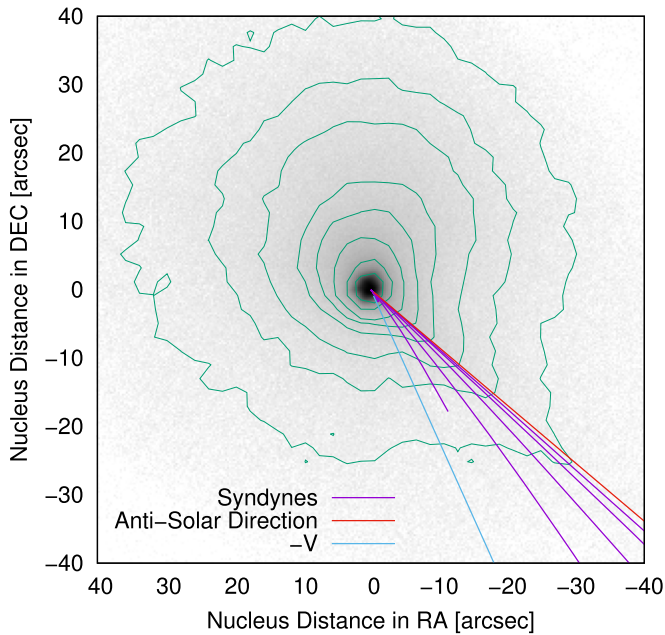
Figure 5. Our 2018 April 25 SOAR observation overplotted with syndynes (lines of constant radiation pressure parameter β, magenta). The syndyne closest to the antisolar direction has $\beta = 0.998$, the following ones have 0.1, 0.01, 10^{-3}, and 10^{-4}, respectively.

The absence of a tail shaped by radiation pressure is reminiscent of, for example, the long-period comet C/2017 K2 (Jewitt et al. 2017, 2019).

In addition to the diffuse coma, our 2018 April 25 SOAR observation shows a narrow tail pointing directly away from the Sun. In this direction, charged particles accelerated by the solar wind would be expected, forming the so-called plasma tail (Ip 2004). Also, recently emitted dust particles, whose trajectories are governed by solar radiation pressure rather than by their initial velocity, would be found in this direction. We have simulated the trajectories of $v = 0$ particles emitted at a range of times and with a range of values for β, and analyzed the lines of constant β ("syndynes") and constant emission time ("synchrones"); (Finson & Probstein 1968, see Figure 5).

We find that the narrow tail is consistent with particles having $\beta \sim 1$. Such particles reach a distance of 40″ (the maximum observed extent of the tail) in about two days and could be either very small (micron-sized) or very porous, or both. If interpreted as a dust tail, this detection could indicate the existence of two groups of dust particles with distinct properties (one large and of typical density, the other either small or porous), of which the second is only detected near perihelion. In situ measurements by the GIADA instrument on board the Rosetta spacecraft have provided hints that such two populations might exist at comet 67P/Churyumov–Gerasimenko (Fulle et al. 2015).

A tail pointing radially away from the Sun was also observed in the Spitzer 4.5 μm channel (but not at 3.6 μm) on 2009 August 22 (Mommert et al. 2014), but a quantitative analysis of the flux ratio was precluded by the low signal-to-noise ratio of the observations.

The two tail observations were obtained at very similar true anomalies (343° in 2009 and 348° in 2018 April). It is possible that both observations show the same phenomenon that repeats around successive perihelion passages. The tail could consist of ions (e.g., CO$^+$ as observed in C/2016 R2 by McKay et al. 2019),

although we point out that the tail observed in Don Quixote lacks the typical filamentary structure of ion tails.

Alternatively, dust can also appear a factor of several brighter at 4.5 μm than at 3.6 μm. For comets at heliocentric distances between 1.2 and 1.3 au, blackbody temperatures between 240 and 257 K have been fit to measurements in the 3–22 μm range obtained with the Wide-field Infrared Survey Explorer (Bauer et al. 2015). In this situation, the 3.6 μm flux is dominated by scattered sunlight, while the 4.5 μm stems mainly from thermal emission and would be a factor 2–3 higher than the 3.6 μm flux, which might already explain the Spitzer observation by Mommert et al. (2014). In addition, small or very porous dust (consistent with $\beta \sim 1$) could display spectra that correspond to even higher blackbody temperatures (Bockelée-Morvan et al. 2017).

3.4. Shape Model and Spin-pole Orientation

We fit a convex shape model to the photometric observations by Skiff et al. (2019) and Mommert et al. (2020) using the lightcurve inversion techniques developed by Kaasalainen & Torppa (2001) and Kaasalainen et al. (2001) and provided as implementation in C by Kaasalainen et al. (2014). Skiff et al. (2019) observed Don Quixote in 2009 November with Lowell Observatory's 0.55 m LONEOS Schmidt telescope and in 2018 August–September with Lowell Observatory's 0.7 m telescope using dense photometric observations; Mommert et al. (2020) observed Don Quixote between 2015 January and 2019 December using sparse observations obtained with a range of telescopes. In the absence of radar observations, lightcurve inversion represents the best method to constrain the spin-pole and shape properties of an asteroid. The shape model generated represents a convex approximation of the true shape of the object, i.e., no large-scale concave features are fit in this model due to the degeneracy that would arise. Lightcurve inversion may also allow for the scattering properties of the object to be determined using a combination of Lambertian and Lommel-Seeliger scattering, however, that is not carried out for Don Quixote due to both the difficulty of obtaining a unique fit to these properties and the effect any activity on the object's surface may have on this fitting.

The model constructs a series of three-dimensional shapes consisting of triangular facets, starting from a triaxial ellipsoid approximation, at a range of different spin states and generates synthetic observations for this object assuming the same viewing geometry as for the real observations. The fit of the synthetic lightcurve obtained from this shape model is compared to the real photometric data. The shape and spin-pole information of the synthetic object is varied and through χ^2 minimization the best-fit parameters for the shape, scattering, and rotational information for the object can be determined.

We find an oblate shape for Don Quixote with the following constraints on pole axis orientation for our best-fit model: ecliptic longitude $\lambda = (71.2 \pm 20)°$, ecliptic latitude $\beta = (-43.9 \pm 20)°$, and rotational period $P = (6.66 \pm 0.02)$ hr, the latter of which perfectly agrees with the period found by Skiff et al. (2019). Figure 6 shows the shape model we derived from our data.

Given the generally low signal-to-noise ratio of the coma in our optical observations (Figure 2), we are unable to identify significant correlations between coma morphology at the different epochs and the pole axis orientation derived here.

Figure 6. Shape model of Don Quixote at four equidistant phase angles over one full rotation. The derived spin-pole axis corresponds to the vertical axis in this representation.

3.5. Active Area

Mommert et al. (2014) derived the diameter of Don Quixote from a range of thermal-infrared observations as $18.4^{+0.3}_{-0.4}$ km, assuming a spherical shape of the object. Sampling the object at different phases, we can assume that the volume of this sphere is very similar to the actual volume of the object. We can take advantage of this measurement and scale the shape model to have a volume that is equivalent to this hypothetical sphere and derive the body's total surface area. We find a total surface area of 1273^{+41}_{-56} km^2 for the scaled convex shape model with uncertainties being propagated from the spherical diameter that do not account for uncertainties from the shape model.

Assuming that the activity observed by Spitzer is driven by the sublimation of CO_2, we can derive the active surface area with a simple sublimation model (Cowan & A'Hearn 1979). We derive the sublimation rate[13] for CO_2 at the heliocentric distance at which Don Quixote was observed by Spitzer as $Z = 4 \times 10^{17}$ molecules cm^{-2} s^{-1} for sublimation at the subsolar point and use this measure as an approximation for the sublimation to be expected for Don Quixote. Scaling the CO_2 production rate we derived from our Spitzer observations (see Section 3.2.1) to this expected sublimation rate, we find an active area of 6500 m^2, which corresponds to 5×10^{-6} of the total convex surface area of Don Quixote (Section 3.4), or a circular patch with a radius of $\sim$45 m.

4. Discussion

4.1. Comparison between Apparitions

We compare the production rates measured from our 2018 Spitzer observation with those measured in 2009 (Mommert et al. 2014). While the CO_2 production rates were calculated using the same assumptions that are used here, we are using different premises for the calculation of the dust production. We revise the results from Mommert et al. (2014) using the same dust grain size, dust velocity and bulk density, and geometric albedo that we use here and find a revised dust production rate upper limit of 0.5 kg s^{-1}. While this change slightly affects the assumed contribution from reflected solar light to the CH2 flux density, which defines the gas production rates, the CO_2 production rate is barely affected by this change and does not require revisions.

Since the 2009 and 2018 apparitions were observed by Spitzer at different heliocentric distances, we can use these observations to check whether the observed production rates scale with heliocentric distance. Assuming that gas production rates (Q) scale with the inverse square of the heliocentric distance (r) at the time of observations (Bauer et al. 2015), we compare the products Qr^2 for both apparitions and find that they indeed agree well within uncertainties. This agreement suggests that activity in Don Quixote is recurrent and not just the result of a recent outburst.

Our ground-based optical observations from the 2018 apparition provide direct measurements of dust activity in Don Quixote that was not observed in 2009, implying either a lack of dust in 2009 or a dust production that was below the detection threshold set by our Spitzer observations. The magnitude of the dust production rates (Section 3.2.3) measured in 2018 is comparable to the revised upper limit that we derived from our 2009 Spitzer data. Comparing the
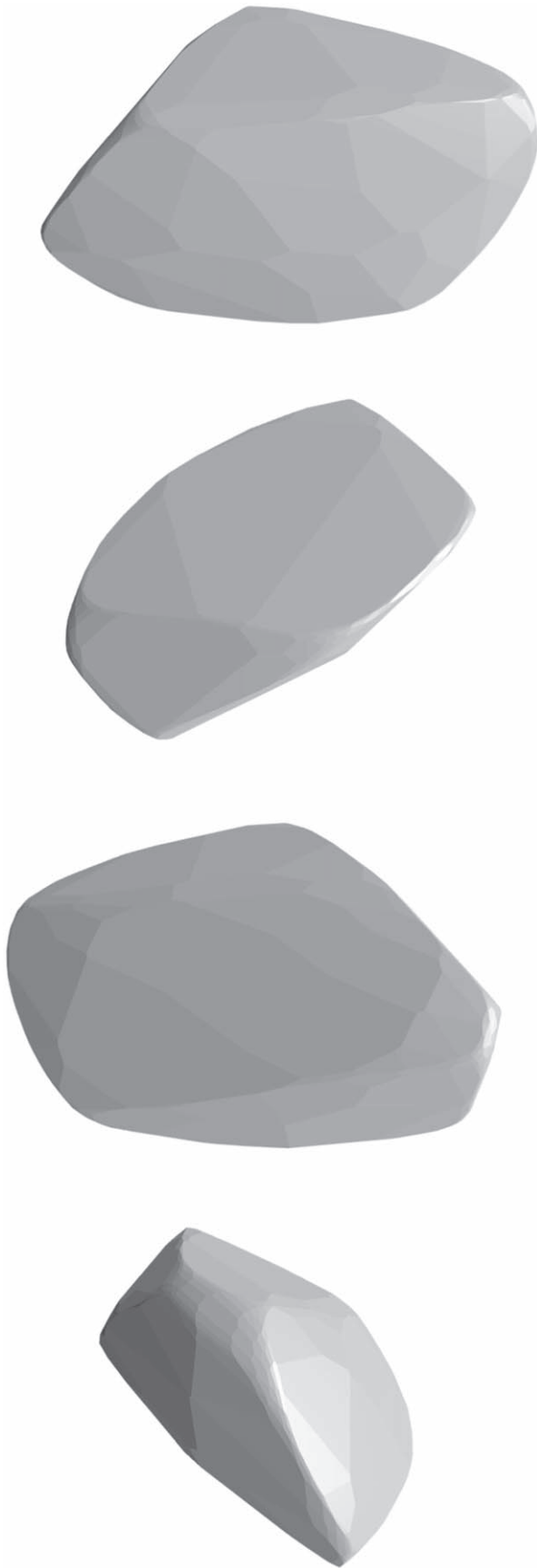
---

[13] https://pds-smallbodies.astro.umd.edu/tools/ma-evap/index.shtml

production rates from our SOAR 2018 April 25 observations with the 2009 Spitzer upper limits—both observations were taken at very similar heliocentric distances—we find that dust production was higher in 2018 by at least a factor of 1.6. While this factor seems significant, we note that estimated dust production rates depend on many assumptions, including the dust velocity and particle size. Minor modifications to these assumptions can easily amount to multiples of the revised dust production upper limit, or even higher. We hence conclude that it is likely that the same dust production rate that was observed in the 2018 apparition might have been present at the 2009 Spitzer observations and might have gone undetected. This finding does not contradict the hypothesis that Don Quixote shows recurrent activity.

4.2. Comparison with Active Comets and Dormant Comets

Both the gas and dust production rates derived for Don Quixote in this work and by Mommert et al. (2014) are low compared to other comets, but not exceptionally low (A'Hearn et al. 1995; Ootsubo et al. 2012; Reach et al. 2013; Bauer et al. 2015). For instance, Schleicher & Knight (2016) report on extremely low activity in comet 209P with $Af\rho$ of the order of 1 cm in the coma and an active surface area fraction of 2.4×10^{-4} (from the sublimation of H_2O). Our optical detections of activity in Don Quixote yield similar values for $Af\rho$ (Section 3.2.3) and an active surface fraction that is two magnitudes lower than for that comet (Section 3.5). While active fractions based on observations of different volatiles (H_2O in 209P and CO/CO_2 in Don Quixote) cannot be directly compared, this effect should be much smaller than two orders of magnitude. Hence, both findings underline the weakness of activity observed in Don Quixote.

Mommert et al. (2020) report on observations of a sample of 75 dormant comet candidates that were taken over more than 4 yr to search for activity in these objects. Although they find a number of dormant comet candidates with surface albedos and spectral behavior similar to Don Quixote in this sample, the only object that showed activity during this program is Don Quixote. None of the other sample targets showed any signs of activity in either the optical or the infrared wavelengths (using Spitzer). If similarly weakly active objects have proportionally smaller active areas, the amount of dust present in their comae might be below detection thresholds.

4.3. The Nature of Activity

The results presented in Section 4.1 suggest that Don Quixote is active during perihelion passages. A recurrent nature of the observed activity is very likely.

The 3σ upper limit on the CO production rate from our IRAM observations (Section 3.2.2) is about four times higher than the hypothetical CO production rate we derive from our Spitzer observations (Section 3.2.1), assuming that the entire observed activity is from CO. Hence, we cannot rule out that our Spitzer observations show molecular band emission from CO instead of CO_2. While other molecules might be present, either CO_2 or CO are most likely to drive the activity observed in Don Quixote.

A comparison of the observations reported in this work and observations reported by Mommert et al. (2014); (see Section 4.1) shows that gas production rates scale inversely with the squared heliocentric distance of the target—a behavior

previously observed for comets by Bauer et al. (2015)—and that dust activity observed around the 2018 apparition roughly agrees with upper-limit estimates from Mommert et al. (2014). Observations agree with an onset of activity when Don Quixote is closer to the Sun than ~ 3 au, which may hint to the presence of H_2O in Don Quixote.

The fact that activity escaped discovery until 2009—although Don Quixote was discovered in 1983—suggests that the level of activity in this object was simply too low to be detected in the past, which is supported by our comparison with other active comets (see Section 4.2).

All these results support the hypothesis that Don Quixote is in fact a weakly active comet instead of a dormant or extinct comet nucleus.

5. Conclusions

We report on observations of Near-Earth object Don Quixote and the repeated discovery of activity in this object. We find activity in the form of a coma from molecular band emission from either CO_2 and/or CO from Spitzer observations when the target was 2.7 au from the Sun. Around the time of the target's perihelion passage, we observed for the first time an optical counterpart to this activity, which we interpret as solar light reflected from dust particles ejected from the surface.

Observations with the 30 m IRAM millimeter radio telescope are unable to rule out CO as the source of the molecular band emission observed by Spitzer.

From a comparison of the gas production rates derived in this work and by Mommert et al. (2014) we find that these scale with the inverse square of the heliocentric distance, suggesting continuous activity in contrast to a short-term outburst. The active surface fraction is extremely small and compatible with a circular patch with a radius of ~ 45 m.

Optical observations indicate the presence of centimeter-sized dust particles in the coma of Don Quixote, as well as a faint narrow tail that is consistent with very small or very porous particles.

All these observations lead us to believe that activity in (3552) Don Quixote is recurrent and that this object is in fact a weakly active comet.

ORCID iDs

Michael Mommert ⓘ https://orcid.org/0000-0002-8132-778X
Joseph L. Hora ⓘ https://orcid.org/0000-0002-5599-4650
David E. Trilling ⓘ https://orcid.org/0000-0003-4580-3790
Kacper Wierzchos ⓘ https://orcid.org/0000-0002-4884-9367
Jessica Agarwal ⓘ https://orcid.org/0000-0001-6608-1489
Yoonyoung Kim ⓘ https://orcid.org/0000-0002-4676-2196
Maria Womack ⓘ https://orcid.org/0000-0003-4659-8653
Matthew M. Knight ⓘ https://orcid.org/0000-0003-2781-6897
Nick Moskovitz ⓘ https://orcid.org/0000-0001-6765-6336
Michael S. P. Kelley ⓘ https://orcid.org/0000-0002-6702-7676

References

A'Hearn, M. F., Feaga, L. M., Keller, H. U., et al. 2012, ApJ, 758, 29
A'Hearn, M. F., Millis, R. C., Schleicher, D. O., et al. 1995, Icar, 118, 223
A'Hearn, M. F., Schleicher, D. G., Millis, R. L., et al. 1984, AJ, 89, 579
Astropy Collaboration, Robitaille, T. P., Tollerud, E. J., et al. 2013, A&A, 558, A33
Bauer, J. M., Stevenson, R., Kramer, E., et al. 2015, ApJ, 814, 85
Bertin, E., Mellier, Y., Radovich, M., et al. 2002, in ASP Conf. Proc. 281, Astronomical Data Analysis Software and Systems XI, ed. D. A. Bohlender, D. Durand, & T. H. Handley (San Francisco, CA: ASP), 228
Binzel, R. P., Rivkin, A. D., Stuart, J. S., et al. 2004, Icar, 170, 259
Bockelée-Morvan, D., Rinaldi, G., Erard, S., et al. 2017, MNRAS, 469, S443
Bottke, W. F., Morbidelli, A., Jedicke, R., et al. 2002, Icar, 156, 399
Brown, A. G. A., Vallenari, A., Prusti, T., et al. 2018, A&A, 616, A1
Burns, J. A., Lamy, P. L., & Soter, S. 1979, Icar, 40, 1

Clemens, J. C., Crain, J. A., & Anderson, R. 2004, Proc. SPIE, 5492, 331
Cowan, J. J., & A'Hearn, M. F. 1979, M&P, 21, 155
Crovisier, J. 1987, A&AS, 68, 223
Crovisier, J., & Encrenaz, T. 1983, A&A, 126, 170
DeMeo, F., & Binzel, R. P. 2008, Icar, 194, 436
Fazio, G. G., Hora, J. L., Allen, L. E., et al. 2004, ApJS, 154, 10
Finson, M. L., & Probstein, R. F. 1968, ApJ, 154, 327
Fulle, M., Della Corte, V., Rotundi, A., et al. 2015, ApJL, 802, L12
Fulle, M., Della Corte, V., Rotundi, A., et al. 2016, MNRAS, 462, S132
Giorgini, J. D., Yeomans, D. K., Chamberlin, A. B., et al. 1996, BAAS, 28, 1158
Hahn, G., & Rickman, H. , 1985, Icar, 61, 417
Hartmann, W. K., Tholen, D. J., & Cruikshank, D. P. , 1987, Icar, 69, 33
Haser, L. 1957, BSRSL, 43, 740
Hora, J. L., Marengo, M., Park, R., et al. 2012, Proc. SPIE, 8442, 39
Hornung, K., Merouane, S., Hilchenbach, M., et al. 2016, P&SS, 133, 63
Hunter, J. D. 2007, CSE, 9, 90
Ip, W.-H. 2004, in Comets II, ed. M. C. Festou, H. U. Keller, & H. A. Weaver (Tucson, AZ: Univ. Arizona Press), 605
Jewitt, D., Agarwal, J., Hui, M., et al. 2019, AJ, 157, 65
Jewitt, D., Hui, M., Mutchler, M., et al. 2017, ApJL, 847, L19
Kaasalainen, M., Ďurech, J., & Sidorin, V. 2014, DAMIT: Database of Asteroid Models from Inversion Techniques, Astrophysics Source Code Library, ascl:1412.004
Kaasalainen, M., & Torppa, J. 2001, Icar, 153, 24
Kaasalainen, M., Torppa, J., & Muinonen, K. 2001, Icar, 153, 37
McKay, A. J., DiSanti, M. A., Kelley, M. S. P., et al. 2019, AJ, 158, 128
Meech, K. J., & Svoreň, J. 2004, in Comets II, ed. M. C. Festou, H. U. Keller, & H. A. Weaver (Tucson, AZ: Univ. Arizona Press), 317
Mommert, M. 2017, A&C, 18, 47
Mommert, M., Hora, J. L., Harris, A. W., et al. 2014, ApJ, 781, 25
Mommert, M., Kelley, M. S. P., de Val-Borro, M., et al. 2019, JOSS, 4, 1426
Mommert, M., Polishook, D., & Moskovitz, N. 2018, CBET, 4502
Mommert, M., Trilling, D. E., Hora, J. L., et al. 2020, PSJ, 1, 10
Ootsubo, T., Kawakita, H., Hamada, S., et al. 2012, ApJ, 752, 15
Pätzold, M., Andert, T., Hahn, M., et al. 2016, Natur, 530, 63
Reach, W. T., Kelley, M., & Vaubaillon, J. 2013, Icar, 226, 777
Rotundi, A., Sierks, H., Della Corte, V., et al. 2015, Sci, 347, 6220
Rudawska, R., & Vaubaillon, J. 2015, P&SS, 118, 25
Samarasinha, N. H., Martin, M. P., & Larson, S. M. 2013, Cometary Coma Image Enhancement Facility (Tucson, AZ: Planetary Sci. Inst.), http://www.psi.edu/research/cometimen
Schleicher, D. G., & Knight, M. M. 2016, AJ, 152, 89
Schuster, M. T., Marengo, M., & Patten, B. M. 2006, Proc. SPIE, 6270, 20
Skiff, B., McLelland, K. P., Sanborn, J. J., et al. 2019, MPBu, 46, 458
Spitzer Science Center 2012, IRAC Instrument Handbook v2.0.2 (Pasadena, CA: IPAC/Caltech), http://irsa.ipac.caltech.edu/data/SPITZER/docs/irac/iracinstrumenthandbook/
Veeder, G. J., Hanner, M. S., Matson, D. L., et al. 1989, AJ, 97, 1211
Werner, M. W., Roellig, T. L., Low, F. J., et al. 2004, ApJS, 154, 1